Proceedings World Geothermal Congress 2020+1
Reykjavik, Iceland, April - October 2021

Implications for the Accuracy of Porosity and Permeability Estimates Derived from X-ray Computed Tomography in Reservoir Characterization

Mathias Nehler[1], Ferdinand Stoeckhert[2], Erik H. Saenger[1,2], Jörg Renner[2], Rolf Bracke[1]

[1]International Geothermal Centre, Lennershofstraße 140, 44801 Bochum

[2]Ruhr-Universität Bochum, Universitätsstraße 150, 44801 Bochum

mathias.nehler@hs-bochum.de

Keywords: X-ray computed tomography, porosity, permeability, flow-through experiments

ABSTRACT

In order to characterize the transport properties for fluids in un-fractured and artificially fractured limestones and porous sandstones, we determined the porosity of those samples by evaluating X-ray tomographic images. Porosity, which is closely related to the hydraulic conductivity, constitutes an important parameter for the primary assessment of deep low to high-enthalpy geothermal reservoirs. The non-destructive CT technique can be used to recreate a virtual three-dimensional model of rock samples from which rock properties, such as porosity, permeability or elastic wave-velocity can be inferred. The results were compared with porosity values deduced from density measurements of the same rock samples. These measurements are constrained by conventional thin section analysis. The porosity measurements are complemented by permeability measurements of artificially fractured sandstones and limestones at various effective pressures using a flow-through apparatus integrated in the X-ray tomography set-up. We used Darcy's law to calculate the absolute permeability and employed the cubic law to estimate the hydraulic aperture of the fractures. Tomographic gray-value images enabled the determination of the geometrical aperture. For either porosity and permeability estimates based on evaluation of the tomographic images, resolution plays a key role and rather precise results were determined for highly, macro-porous samples and highly permeable fractures with apertures exceeding $3 \cdot 10^{-4}$ m.

1. INTRODUCTION

The characterization of hydrocarbon and geothermal reservoirs relies on an accurate determination of geophysical rock properties, such as porosity and permeability. The fluid flow in porous and fractured rocks is of high interest for numerous applications including geothermal energy production. However, the fluid flow in fractured, anisotropic systems is still poorly understood and understanding of fracture permeability is still a challenging topic in subsurface flow (Tokan-Lawal et al., 2015).

X-ray computed tomography (CT) offers a destruction less opportunity to derive porosity and permeability or electrical current flow to quantify resistivity and elastic deformation to quantify elastic moduli and the elastic-wave velocity (Andrä et al., 2013) from the reconstructed images. The X-rays pass through a solid object and became attenuated with respect to material density. The intensity of the attenuated X-rays are measured by a detector array under different angles (Knoll, 2000). Computer algorithms enable the reconstruction of 3D images using the measured 1D projection of X-ray intensities for a scanned object (Kak and Slaney, 2001).

The tomographic images were segmented into open pore space and minerals to calculate the total porosity of the binary images. Various unsupervised, global segmentation methods were implemented to calculate porosity with respect to a.) rock type and b.) resolution. The effect of resolution was examined by using three different diameters of the cylindrical samples of 3, 10, and 30 mm, corresponding to voxel sizes of 2.4, 8.0 and 22 µm, respectively. We determined the total porosity from the ratio between bulk and matrix density to access the accuracy of the porosity values derived from the tomographic images.

The transport properties of reservoir rocks depend not only on total porosity, but also on the spatial arrangement of open pore space features and their individual characteristics. Consequently, porosity characterization was complemented by flow-through experiments in an X-ray micro-tomography scanner at elevated pressures. The pressure-dependent permeability was derived only for low-porosity samples with single fractures oriented parallel to the flow direction to restrict fluid flow to the fracture. The effective permeability was calculated from steady-state flow based on Darcy's law. The mean fracture aperture was derived from the intensity images and used to estimate fracture permeability according to the cubic law. Monitoring the evolution of porosity and permeability with the state of stress in quasi time-resolved flow-through experiments enhances our understanding of flow processes in porous or fractured media on the microscale. Understanding the interplay of fluid flow and geomechanical processes at the microscale will help to upscale these phenomena to enhance the efficiency of large scale geothermal applications, i.e. by increasing the transport properties for fluids.

2. METHODOLOGY

We determined the total porosity and connected porosity. The total porosity $\emptyset_{\mathrm{tot,lab}}$ calculates from the ratio between bulk density ρ_{b} and matrix density ρ_{m} according to

$$\emptyset_{\mathrm{tot,lab}} = 1 - \frac{\rho_{\mathrm{b}}}{\rho_{\mathrm{m}}}. \quad (1)$$

The samples with a diameter of 30 mm were used to determine the bulk density by weighing after drying at 60°C for 24 hours and the geometrical estimation of the bulk volume V. A capillary pycnometer was used to determine the matrix density as described in the DIN 18124. The powder was produced with a ball mill and sieved afterwards. For determination of the connected porosity $\emptyset_{\mathrm{con,lab}}$

a dry rock was weighed prior to saturation to determine the sample mass m_{dry}. The weight of the saturated sample m_{wet} was determined after removing the excess fluid from the surface of the sample. The connected porosity calculates according to

$$\emptyset_{\mathrm{con,lab}} = \frac{m_{\mathrm{sat}} - m_{\mathrm{dry}}}{\rho_{\mathrm{H2O}} V}. \quad (2)$$

Additional fractured samples were either prepared with 'smooth' saw-cut slits to mimic parallel fracture surfaces or were induced artificially. We glued the samples together and cured them for at least 24 hours. Afterwards, cylindrical cores with a diameter of 10 mm were diamond-drilled with the cylindrical axis parallel to the fracture plane. The samples were cut and ground to a length-to-diameter ratio of about 2.5. Finally, the glue was dissolved by submerging the samples in Acetone for at least 24 hours.

Unidirectional flow-through experiments in single fractures were conducted an X-ray transparent core holder consisting of aluminum (Niemi et al., 1997; Raven and Gale, 1985; Souley et al., 2015). The modular based assembly allows for easy exchange of parts and an adaption for (long-term) flow-through experiments inside the X-ray CT scanner. Sample size is limited to diameters of 10 mm, while the sample length is between 20 and 30 mm. The cylindrical samples and porous spacers at either end were placed in a Viton sleeve. The pressure cell is placed inside the X-ray computed tomography system on the rotational stage (Figure 1). The confining pressure is controlled by the water pressure surrounding the sample in the annulus between sleeve and the aluminum tube. We used a confining pressure level of at least 2.5 MPa to prevent flow between the Viton sleeve and the sample. The confining pressure level was always kept larger than the pore pressure level. We performed the experiments at pressures between 2.5 and 30 MPa to simulate reservoir conditions corresponding to a depths of around 1000 m. The samples were constrained in axial direction. Darcy's law was used to determine the permeability k_{hyd} by measuring the pressure gradient Δp, the flow rate Q, the sample length L and the sample radius r according to

$$k_{\mathrm{hyd}} = \frac{\eta L Q}{\pi r^2 \Delta p}, \quad (3)$$

where η denotes the dynamic fluid viscosity.

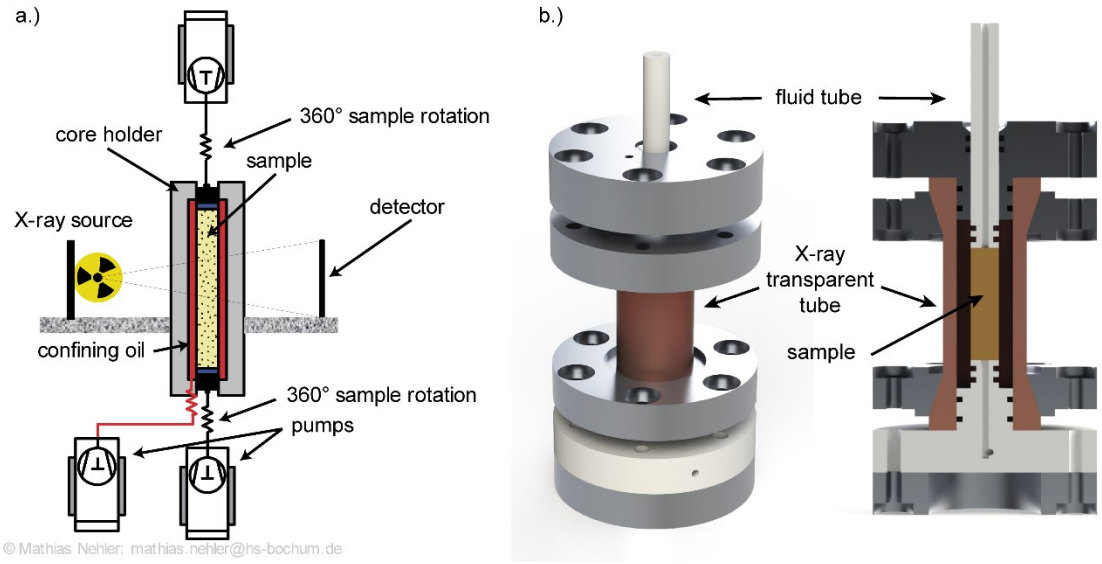

Figure 1: a.) Simplified sketch of the experimental setup for in-situ flow-through experiments. b.) Computer-aided design of the newly developed core holder.

A computed micro-tomography (CT) scanner equipped with a multifocal X-ray tube with a maximum acceleration voltage of 225 kV and 50 W power output was used to image the samples. The samples were positioned in between the X-ray tube and the detector. Because the field of view is limited by the distances between the X-ray source and the sample as well as the X-ray source and the detector the achievable resolution, i.e. the voxel size increases with decreasing sample diameter. The highest resolution of about 2.5 µm yield samples with a diameter of 3 mm. Acceleration voltage, current and exposure time were optimized with respect to the detector sensitivity.

The reconstruction process is based on a Radon transform (Feldkamp et al., 1984) and was performed with the Volex reconstruction engine (Fraunhofer-Allianz Vision, 2012). The result is represented by discretized cubic volume elements, termed *voxels*, in the reconstructed images. The measured intensity values represent the local X-ray attenuation coefficients, which are computed for each voxel and associated with its location in three-dimensional space. The three-dimensional intensity data is usually visualized using a gray-scale color range, in which dark and bright voxels indicate low and high attenuation, respectively.

After reconstruction nine cuboid subvolumes were extracted from the tomographic datasets. Subvolumes were used to reduce computational time and to avoid the sample rims affected most by beam hardening artefacts (Figure 2). Quantitative characterization of pore space features requires the conversion of the gray-scale images into binary images by partitioning an image, a process called image segmentation (e.g. Gros, 2010). Only global segmentation methods, which define absolute threshold values for the entire image, were used to define those classes. For the calculation of porosity, the images were segmented into two classes, solid material and pore space, separated by a single threshold value. Porosity Φ_{CT} calculates then as the ratio of the segmented pore space volume

to the complete (sub-) volume. Strictly speaking Φ_{CT} is defined as the volume fraction of voids within the total examined subvolume. Applied segmentation algorithms are (FR) fixed ratio, based on a used defined ratio to select a threshold value, (MV) maximum variance (Otsu, 1979), (UM) unimodal (Rosin, 2001), (ME) minimum error (Kittler and Illingworth, 1986), (KM) k-means (Ridler and Calvard, 1978), (SH) shape (Tsai, 1995) and (MP) mid-point (Saenger et al., 2016). Only unfiltered datasets are used to compare the various thresholding methods.

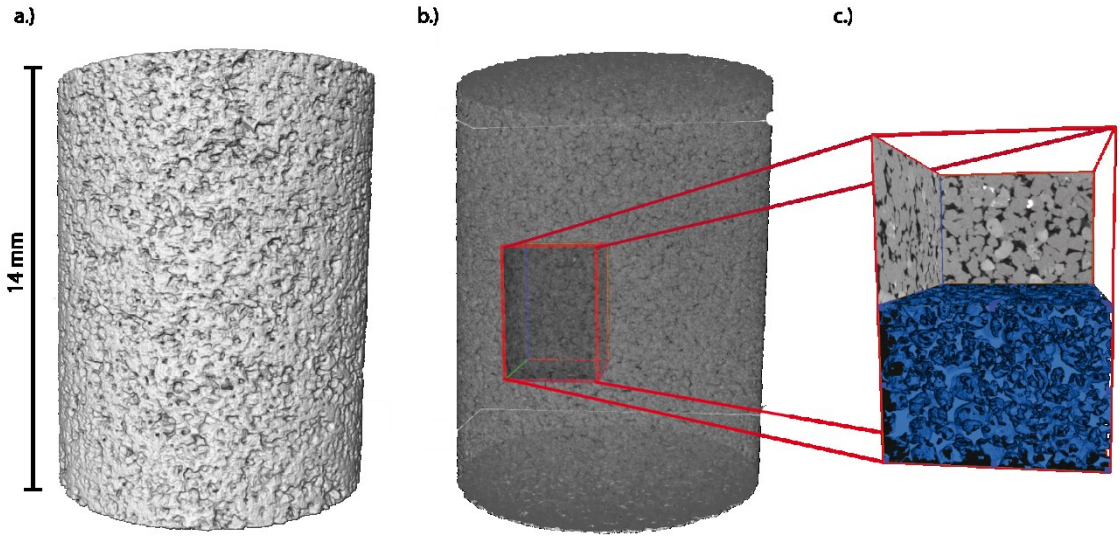

Figure 2: a.) Three dimensional representation of Pfaelzer sandstone using X-ray computed tomography, b.) extracted subvolume and, c.) pore space visualization (blue) after segmentation.

Segmentation of the fractured samples involved an additional step using a connectivity filter. The three-dimensional connectivity filter determines the largest component by looking at the neighbors of every voxel touching that specific voxel either at one of the faces, edges, or corners, assuming to be part of the fracture (Toriwaki and Yoshida, 2009). Afterwards the fracture aperture was determined using a maximum sphere approach (Mourzenko et al., 1995) in two dimensions perpendicular to the flow direction implemented in *Matlab*. Employing the cubic law (e.g. Witherspoon et al., 1980) enabled the calculation of a geometrical permeability k_{CT}. For a pair of smooth, parallel plates and laminar flow conditions the cubic law provides an analytical solution according to

$$Q = \frac{Dw^3 \Delta p}{12 \eta L}, \tag{4}$$

where w denotes the aperture, L the sample length and D the width of the fracture, perpendicular to the fracture gradient (Figure 3). A geometrical fracture permeability k_{CT} can be calculated using the mean fracture aperture w_{geo} according to

$$k_{CT} = \frac{w_{geo}^2}{12}, \tag{5}$$

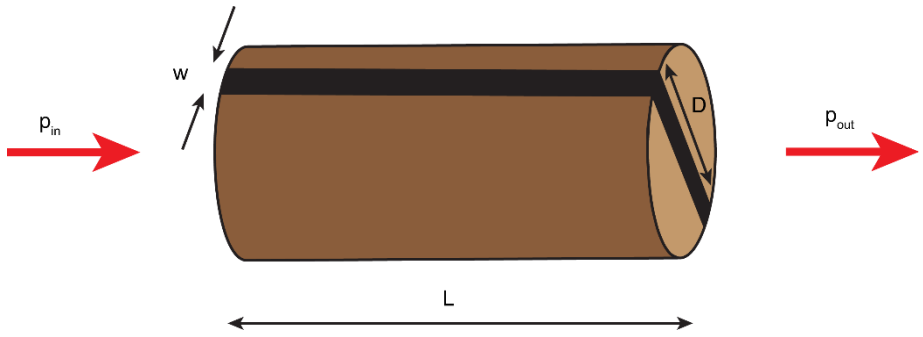

Figure 3: Sketch illustrating the parameters of the cubic law.

3. SAMPLES

Porosity was examined for eight different quartz-rich sandstones. Berea sandstone (B), Bentheim sandstone (GBS) and Pfaelzer sandstone (PS), which represent typical siliciclastic hydrocarbon reservoir rocks, while Wilkeson sandstone (WS), Oberster sandstone (OS) or Ruhr sandstone (GR) represent arkoses with highly variable mineralogical composition and lower porosities due to the deposition in a fluvio-deltaic environment (Figure 4). Fontainebleau sandstone is characterized by quartz content of nearly 100 %, while other samples, such as Wilkeson sandstone have a quartz content of around 40 %. Feldspars, mica and clay minerals represent

secondary components with a highly variable amount. The examined Fontainebleau sandstones (FS) are fine grained quartz arenites of intermediate porosity between 5 and 15 %.

Permeability of single fractures was determined for the low porous Ruhr sandstone, but also for limestone samples originating from a low-enthalpy geothermal reservoir near Turnhout, which is located in the province of Antwerp, Belgium. The sample originates from the Turnhout well with a depth of 2355 m. The often karstified limestone was deposited during the Dinantian in a sequence of limestone and dolomites. The rock is generally compact, but locally traversed by permeable veins and fault zones resulting in high permeability (Figure 4).

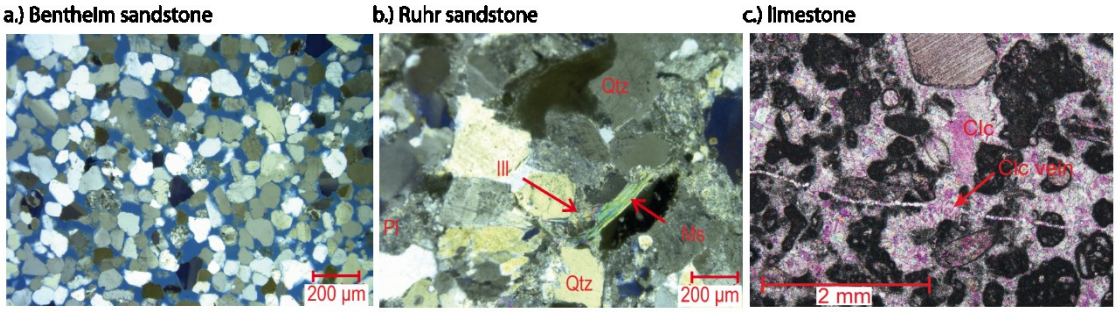

Figure 4: Thin section photomicrographs show Bentheim sandstone, Ruhr sandstone and Turnhout limestone under cross-polarized light. Minerals abbreviated by (ill) illite, (ms) muscovite, (pl) plagioclase, (qtz) quartz and (clc) calcite. The sample of Bentheim sandstone was dyed with a blue resin to show the porosity.

4. RESULTS

Total porosity $\Phi_{tot,lab}$ is between 3 and 23 % for the sandstones. Connected porosities $\Phi_{con,lab}$ derived from water imbibition are smaller than the measured total porosities $\Phi_{tot,lab}$. The total porosities $\Phi_{tot,CT}$ calculated by evaluating the tomographic images range from about 2 % to nearly 25 %. However, the tested global thresholding algorithms show largely different results for porosity. Measured porosity differs by up to more than 20 % in case the resolution of the tomographic images was significantly smaller than the mean pore size. In contrast, increasing resolution enables rather accurate porosity estimates. Particularly, the total porosities of Berea, Bentheim and Pfaelzer calculated from the tomographic images are similar to the porosities derived from density measurements. These rocks are characterized by quite large equivalent mean pore diameters of about 30 µm. Furthermore, most of the open pores are connected in Berea, Bentheim and Pfaelzer sandstone (Figure 5). The amount of isolated voids increases for the suite of Fontainebleau sandstones. However, there is still a clear connectivity of the pore network important for the flow of fluids. In contrast, Wilkeson, Oberster and Ruhr sandstone are mainly comprised of isolated voids preventing larger fluid-flow.

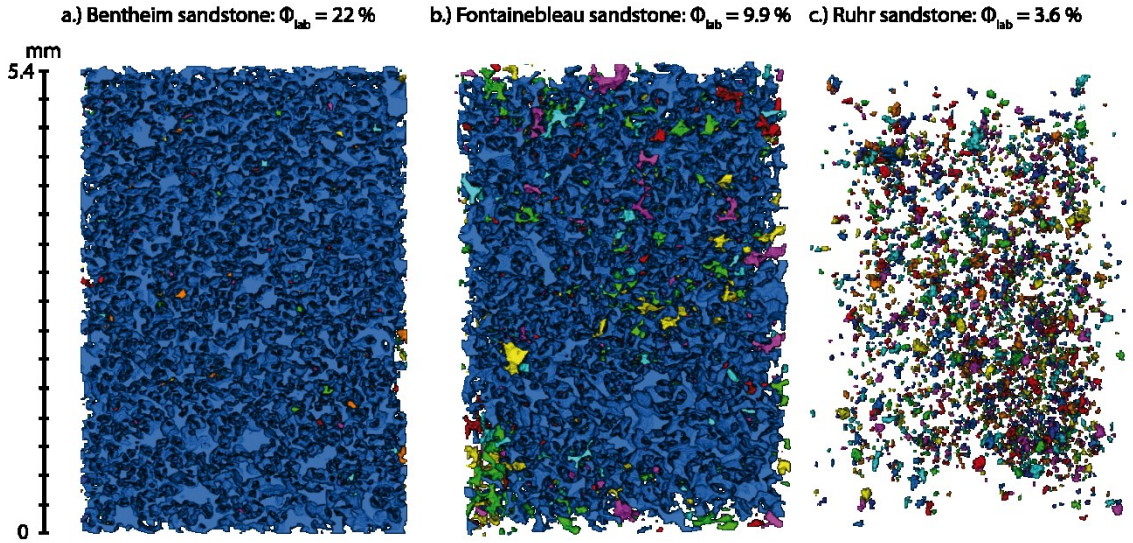

Figure 5: Segmented and visualized open pore space features at a resolution of 8 µm for a. Bentheim sandstone b.) Fontainebleau and c.) Ruhr sandstone. The large blue component shows the connected pores useable for the transport of fluids, while multi-colored labels indicate isolated voids.

The measured intensity distributions of the X-ray attenuation coefficients of the reconstructed images reflect the differences in total porosity, but also in mineralogical composition as well as the geometrical shape and size of the pore space features. The dominant mode of the distribution of X-ray coefficients can be attributed to the solid grains in the reconstructed intensity images (Figure 6). The secondary peak with a lower mode value represents the X-ray attenuation coefficients of the open pore space, such as voids or

open fractures. However, tomographic images of the sandstones show only unimodal or skewed intensity distributions instead of bimodal intensity distributions.

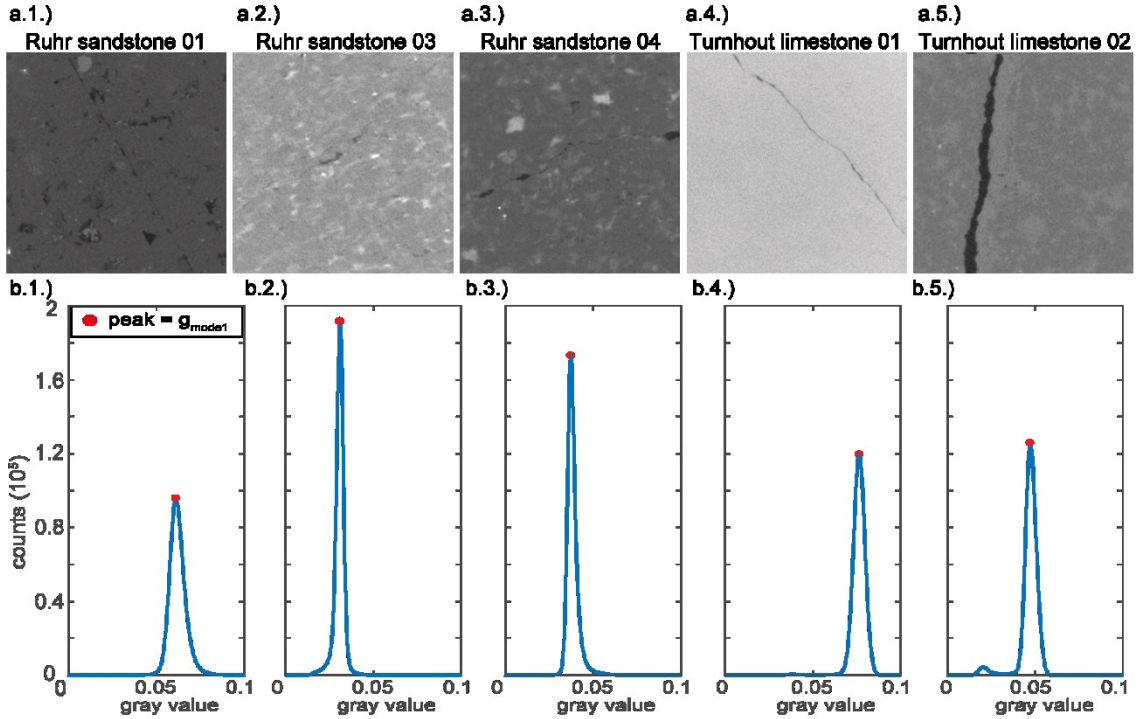

Figure 6: The figure shows a.) the unfiltered gray-value images and b.) the corresponding measured intensity distribution of the fractured Ruhr sandstone and Turnhout limestone samples used for flow through experiments. Only Turnhout limestone 02 (subplot b.5.) shows a clear bimodal intensity distribution. Images were taken at confining pressures of 5 MPa.

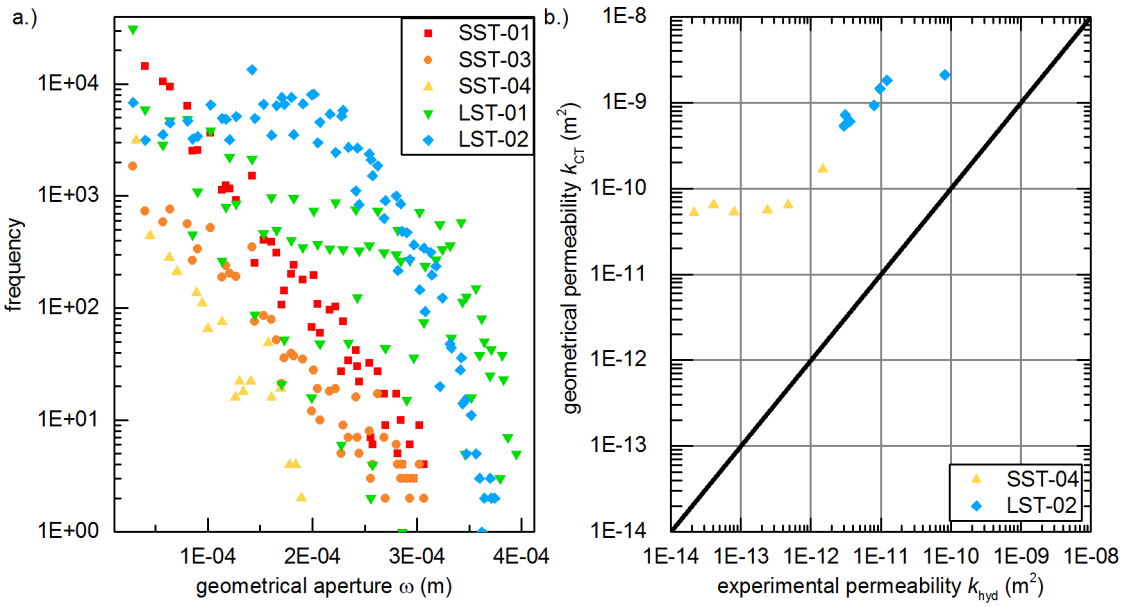

Figure 7: a.) Frequency of geometrical apertures at a confining pressure of 5 MPa deduced from the tomographic images illustrated in Figure 6 and b.) comparison between experimental permeability k_{hyd} and geometrical permeability k_{CT}. Subplot b.9 shows the pressure dependent permeability for limestone sample 02 and sandstone sample 04 characterized by the highest and lowest permeability, respectively.

We determined arithmetic mean values for the apertures ranging from $1.6 \cdot 10\text{-}4$ m^{-4} to $4.5 \cdot 10\text{-}5$ m^{-5}. The examined limestone samples are characterized by a higher amount of larger, continuous apertures than in the fractured samples of Ruhr sandstone (Figure 7). The permeability estimates based on the mean value for the geometrical apertures employing the *cubic law* overestimate permeability compared to experimentally determined permeability (Figure 7). A systematic pressure dependence is only given for the limestone sample (Figure 7).

5. DISCUSSION

Unimodal or skewed intensity distributions hinder segmentation significantly. Consequently, the distinction between empty pores and solid grains is not straightforward and porosity derived from the CT images does not match porosity calculated from bulk and grain density measurements. Tracing the fractures and segmenting them was successful for large fractures in a homogeneous, non-porous matrix as true for the limestone. However, fracture extraction from the segmented binary images is not straightforward for sandstone samples characterized by a complex mineralogical composition, inhomogeneity, fine structures and a porous matrix. The uncertainty for the determination of geophysical rock properties, such as porosity, increases. Generally, it can be expected that macroscopic fractures with apertures above $5 \cdot 10^{-4}$ m representing major flow paths in geothermal systems, could be recognized even for cores with diameters of around 30 mm.

We compared the hydraulic aperture to the normalized mean value of the geometrical aperture derived from evaluating gray-value images. It is expected that at large separation distances both approximately coincide with each other resulting in identical permeability. By employing the cubic law we show that the pressure dependence for permeability is reproduced provided that the resolution is sufficient and that effects such as surface roughness and tortuosity play a subordinate role. For increasing normal stresses, apertures decrease. The flow becomes more tortuous and roughness as well as contact areas increase non-linearly with increasing pressure. Monitoring these processes or the development of scalings at the microscale requires very high resolutions to ensure accurate segmentation of the desired features, which are often in the range of a few micrometer or even in nanometer scale. Many lab based computed tomography systems with a maximum resolution of around 1 µm cannot fulfil these requirements satisfactorily especially for larger sample diameters.

6. CONCLUSIONS

Porosity was determined for various sandstones using density measurements and tomographic images. By increasing the sample diameter the resolution decreases increasing the inaccuracy for porosity determination. For the geometrical characterization of fractures the resolution plays an equally important role as for porosity. The limited resolution of X-ray computed micro-tomography can result in non-resolved apertures that in turn lead to erroneous permeability estimates when estimating the permeability by employing the cubic law compared to experimentally determined permeability.

The results indicate, that the resolution of lab based computed-tomography systems is usually sufficient for direct estimations of porosity and permeability values in case of macro-porosity, macro-fractures or fracture networks with features of hundreds and more micrometers, which represent the major flow-path in geothermal reservoirs. In contrast, porosity evaluation is not straight forward for micro-porosity, micro-fractures or dual porosity due (partly) unresolved structures. Advanced experimental methods, such as dual energy scans and newly developed segmentation algorithm, such machine learning, could potentially improve the determination of rock properties under these circumstances.

REFERENCES

Andrä, H., Combaret, N., Dvorkin, J., Glatt, E., Han, J., Kabel, M., Keehm, Y., Krzikalla, F., Lee, M., Madonna, C., Marsh, M., Mukerji, T., Saenger, E.H., Sain, R., Saxena, N., Ricker, S., Wiegmann, A., Zhan, X., 2013. Digital rock physics benchmarks—Part I: Imaging and segmentation. Computers & Geosciences 50, 25–32.

Feldkamp, L.A., Davis, L.C., Kress, J.W., 1984. Practical cone-beam algorithm. J. Opt. Soc. Am. A 1 (6), 612.

Fraunhofer-Allianz Vision, 2012. Volex: Volume Explorer Software. Fraunhofer IIS, Fürth, Germany.

Gros, X.E. (Ed.), 2010. NDT data fusion. Arnold, London, New York, New York, 205 pp.

Kak, A.C., Slaney, M., 2001. Principles of computerized tomographic imaging. Classics in applied mathematics 33. Society for Industrial and Applied Mathematics, Philadelphia, 327 pp.

Kittler, J., Illingworth, J., 1986. Minimum error thresholding. Pattern Recognition 19 (1), 41–47.

Knoll, G.F., 2000. Radiation detection and measurement, 3rd ed. ed. Wiley, New York, 802 pp.

Mourzenko, V.V., Thovert, J.-F., Adler, P.M., 1995. Permeability of a single fracture; validity of the Reynolds equation. J. Phys. II France 5 (3), 465–482.

Niemi, A.P., Vaittinen, T.A., Vuopio, J.A., Pöllä, J.P., 1997. Simulation of heterogeneous flow in a natural fracture under varying normal stress. International Journal of Rock Mechanics and Mining Sciences 34 (3-4), 227.e1-227.e11.

Otsu, N., 1979. A threshold selection method from gray-level histograms. IEEE Trans. Syst., Man, Cybern. 9 (1), 62–66.

Raven, K.G., Gale, J.E., 1985. Water flow in a natural rock fracture as a function of stress and sample size. International Journal of Rock Mechanics and Mining Sciences & Geomechanics Abstracts 22 (4), 251–261.

Ridler, T.W., Calvard, S., 1978. Picture thresholding using an iterative selection method. IEEE Trans. Syst., Man, Cybern. 8 (8), 630–632.

Rosin, P.L., 2001. Unimodal thresholding. Pattern Recognition 34 (11), 2083–2096.

Saenger, E.H., Lebedev, M., Uribe, D., Osorno, M., Vialle, S., Duda, M., Iglauer, S., Steeb, H., 2016. Analysis of high-resolution X-ray computed tomography images of Bentheim sandstone under elevated confining pressures. Geophysical Prospecting 64 (4), 848–859.

Souley, M., Lopez, P., Boulon, M., Thoraval, A., 2015. Experimental hydromechanical characterization and numerical modelling of a fractured and porous sandstone. Rock Mechanics and Rock Engineering 48 (3), 1143–1161.

Tokan-Lawal, A., Prodanović, M., Eichhubl, P., 2015. Investigating flow properties of partially cemented fractures in Travis Peak Formation using image-based pore-scale modeling. J. Geophys. Res. 120 (8), 5453–5466.

Toriwaki, J., Yoshida, H., 2009. Fundamentals of three-dimensional digital image processing. Springer, London, XV, 286 S.

Tsai, D.-M., 1995. A fast thresholding selection procedure for multimodal and unimodal histograms. Pattern Recognition Letters 16 (6), 653–666.

Witherspoon, P.A., Wang, J.S.Y., Iwai, K., Gale, J.E., 1980. Validity of cubic law for fluid flow in a deformable rock fracture. Water Resour. Res. 16 (6), 1016–1024.